Available online at www.sciencedirect.com
SCIENCE DIRECT
Polymer 46 (2005) 11359–11365
polymer
www.elsevier.com/locate/polymer

Crystallization behavior of polymer/montmorillonite nanocomposites. Part I. Intercalated poly(ethylene oxide)/montmorillonite nanocomposites

Douwe Homminga [a], Bart Goderis [a], Igor Dolbnya [b], Harry Reynaers [a], Gabriel Groeninckx [a,*]

[a] *Laboratory of Macromolecular Structural Chemistry, Division of Molecular and Nanomaterials, Department of Chemistry, Catholic University of Leuven (KULeuven), Celestijnenlaan 200F, 3001 Heverlee, Belgium*
[b] *Dubble CRG/ESRF, rue Jules Horowitz, c/o BP 220 F38043, France*

Received 25 March 2005; received in revised form 1 August 2005; accepted 4 October 2005
Available online 27 October 2005

Abstract

The influence of montmorillonite (MMT) silicate layers on the semicrystalline morphology development of the poly(ethylene oxide) (PEO) matrix of PEO/MMT nanocomposites has been investigated by using X-ray diffraction, differential scanning calorimetry, light microscopy and time-resolved simultaneous small- and wide-angle X-ray scattering. The silicate layers act as nucleating agents for the crystallization of PEO, but at high contents also have a retarding effect on the crystal growth. In that case they are non-crystallisable barriers in the crystallization of the PEO matrix. The lamellar semicrystalline structures of pure PEO and the PEO/MMT nanocomposites are, however, identical.

Keywords: Poly(ethylene oxide); Nucleating agent; Nanocomposite

1. Introduction

Nanocomposites based on polymers and layered silicates have attracted much interest in the last decade since such polymer-layered silicate nanocomposites (PLSN) display a considerable enhancement of strength, modulus, gas barrier resistance and heat distortion temperature compared to their pure polymer counterparts [1–7]. This enhancement is already obtained with silicate loadings as low as 1–4 vol%. PLSN are scientifically interesting because of the new nano-scale constraints of the filler to the polymer matrix and the ultra-high specific interfacial area between the silicate and the matrix.

Two types of PLSN are known: intercalated and exfoliated nanocomposites. In the former case the polymer chains are inserted in between the silicate layers, thereby increasing the silicate layer interlayer distance of the stacks of the original clay structure without destroying them. In the exfoliated case the silicate layers are uniformly dispersed over the polymer matrix and the stacks of the original clay structure are delaminated.

In the last decade, the main focus of research has been on the synthesis, characterization and physical properties of PLSN. However, in recent years, other topics such as the crystallization behavior of the matrix polymer have attracted more and more attention. In crystallization behavior studies on PLSN, the most studied matrix polymer was either polyamide-6 (PA-6) or polypropylene (PP). In the case of PA-6 nanocomposites, the main focus has been on the influence of the silicate layers on the polymorphic crystal structures of PA-6. However, a full and generalized understanding of the effects of silicate layers on the crystallization behavior of the polymer matrix in nanocomposites has not been reached yet.

Silicate type minerals, like talc and mica, are well-known nucleating agents [8,9]. So, these nano-sized silicate layers may well act as nucleating agents in the crystallization of the polymer matrix of PLSN. This effect on nucleation, resulting in higher crystallization rates, has been observed recently [3,6,10–19].

Furthermore, besides the influence on nucleation, a retarding effect of the silicate layers on the crystal growth of

* Corresponding author. Tel.: +32 16 327440; fax: +32 16 327990.
E-mail address: gabriel.groeninckx@chem.kuleuven.ac.be (G. Groeninckx).

0032-3861/$ - see front matter © 2005 Elsevier Ltd. All rights reserved.
doi:10.1016/j.polymer.2005.10.016

polymer matrices has been found [20–23]. In the crystallization of extruded PA-6/MMT nanocomposites, the overall crystallization rate decreases with increasing silicate layer content at the highest silicate layer contents, or even over the full silicate layer content range [20]. However, processing easily masks this effect. The PA-6 crystallization temperature increases with ~15 °C after extrusion. This is known as the memory effect and has been attributed to the break-up of a H-bond stabilized disordered structure in virgin PA-6 [24,25]. Hence, this decrease in overall crystallization rate only becomes apparent when extruded PA-6/MMT nanocomposites are compared to extruded pure PA-6. It was postulated that during the crystallization of the matrix polymer, the silicate layers act as non-crystallisable barriers. These barriers, especially at high concentration, disturb crystal growth by forcing the growing lamellar stacks along a more tortuous growth path and can possibly even stop several from growing. Another possibility is that the silicate layers hinder polymer chain motion [20] as mentioned earlier by Lincoln et al. [3].

In this study, poly(ethylene oxide) (PEO) was selected as the matrix polymer. PEO finds applications that take advantage of the high viscosity of its aqueous solution. This includes flocculation, denture adhesives, packaging films (pesticides, herbicides, seed tapes), thickening of acid cleaners and water-based paints, and friction reduction. There is also considerable effort aimed at using ethylene oxide polymers and copolymers complexed with ionic salts as the electrolyte in all-solid rechargeable batteries [26]. PEO is a crystallisable polymer with a crystallinity around 65%, a glass transition temperature of −67 °C [27] and a melting temperature of 65 °C.

The present investigation aims at unraveling the influence of the silicate layers on the PEO semicrystalline morphology development. The MMT contents of the melt extruded PEO/MMT nanocomposites were 1, 2, 4 and 10 wt%, respectively. The silicate morphology of the PEO/MMT nanocomposites was assigned by X-ray diffraction. Differential scanning calorimetry (DSC) was used to evaluate the mass crystallinity development. The growth of the spherulitic morphology was followed with light microscopy (LM), and the development of the lamellar semicrystalline structure and the order of the crystal lattice were investigated by small- (SAXS) and wide-angle (WAXS) X-ray scattering, respectively.

2. Experimental

2.1. Materials

Nanocomposites were prepared by melt mixing montmorillonite (Cloisite 15A, dimethyldioctadecylammonium ions as surfactants, Southern Clay products, Gonzales, USA) with poly(ethylene oxide) (M_v = ca. 300,000 g/mol, Aldrich Chemical Company, Inc., USA). Melt mixing was performed in a co-rotating twin-screw mini-extruder (designed by DSM Research, The Netherlands) at 90 °C for 15 min at a mixing rate of 65 rotations/min and under nitrogen atmosphere. The MMT loadings were 1, 2, 4 and 10 wt%, respectively. Pure PEO was also melt extruded for a correct comparison although no differences in crystallization behavior could be observed between virgin and extruded PEO.

2.2. X-ray diffraction

X-ray scattering measurements were performed at the Dutch-Belgian Beamline (DUBBLE) on the European Synchrotron Radiation Facility (ESRF) in Grenoble, France.

In the first set-up, used for assigning the PSLN morphology, static X-ray diffraction patterns were collected for 5 min at room temperature, using an X-ray wavelength of 0.7294 Å and a 2D multiwire detector at 1.25 m from the sample position, covering the range $0.074 \leq s \leq 0.701$ nm^{-1} (with $s = 2 \sin \theta/\lambda$, 2θ being the scattering angle and λ the wavelength). Linear patterns were obtained after averaging azimuthally. The scattering angles were calibrated using silver behenate and converted to angles that correspond to the wavelength of Cu Kα-radiation.

In the second set-up, time-resolved and simultaneous SAXS and WAXS experiments were conducted using a wavelength of 1.1273 Å. Data were collected on a quadrant detector for SAXS at 3 m from the sample position, covering the range $0.0355 \leq s \leq 0.174$ nm^{-1}, and a microstrip line detector for WAXS, covering the angular range $7.7 \leq 2\theta \leq 66°$. The scattering angles were calibrated using silver behenate and collagen (SAXS) and silicon (WAXS). Samples were mounted in copper holders and a Linkam hot stage was used for the temperature control. After melting at 100 °C for 2 min the samples were brought to 48 °C at 10 °C/min for isothermal crystallization. Data collection was started on reaching the isothermal temperature for 40 min over consecutive acquisition time lapses of 15 s. The WAXS and SAXS intensities were normalized to the intensity of the primary X-ray beam and corrected for the detector response.

2.3. Differential scanning calorimetry (DSC)

Isothermal DSC measurements were performed on a Perkin Elmer DSC 7, calibrated with the melting point of indium (156.6 °C) and benzophenone (48.1 °C) for the temperature and with indium for the enthalpy (28.45 J/g). The exothermic crystallization heat was registered isothermally at 48 °C and after normalization to the PEO mass (not the sample mass, since the MMT mass contribution is irrelevant to the PEO crystallinity) converted to a PEO crystallinity using a reference Δh_f value of 197 J/g for the melting of 100% crystalline PEO [27]. Before cooling to 48 °C at 40 °C/min, the samples were kept at 100 °C for 5 min.

2.4. Light microscopy (LM)

Polarized light microscopy images were collected on a digital CCD camera (JVC TK-C1381) during the isothermal crystallization at 48 °C. The microscope used was an Olympus BH-2. The samples were thin films of approximately 50 μm, melt pressed between two glass cover slips. The temperature of

the samples was controlled by a Mettler FP82HT hot stage. Samples were molten at a temperature of 100 °C for 5 min and then brought to 48 °C at 10 °C/min. Spherulite radii were determined as a function of time and converted into spherulite growth rates using a script within the Leica Qwin Image Analysis software program.

3. Data analysis

3.1. Small-angle X-ray scattering (SAXS)

An averaged melt pattern was subtracted as a background from the time-resolved SAXS patterns, collected using the second setup. In this way also the contribution to the scattering patterns by the morphology of (as will be shown below) intercalated silicates in the PEO matrix is effectively discarded, except for the sample with 10% MMT for which this contributions was too dominant. Accordingly this sample was not considered in the X-ray work. This part of the structure as well as the corresponding electron density contrast between the silicate stacks and the surrounding semicrystalline regions is considered to be constant, neglecting the small change and densification of the PEO phase upon crystallization.

After a suitable extrapolation to zero and high angles [28] linear correlation functions, $K(x)$, were calculated by cosine transformation:

$$K(x) = \int_0^\infty I(s)s^2\cos(2\pi xs)\mathrm{d}s \tag{1}$$

The (relative) invariant of the corresponding ideal two-phase structure, Q_{id}, was obtained from the intercept of the linear regression to the autocorrelation triangle [29] and—with the silicate contribution subtracted—was interpreted in the framework of a model that assumes the presence of semicrystalline regions in an amorphous matrix [28]:

$$Q_{id} = C\alpha_S\phi_L(1-\phi_L)(d_c-d_a)^2 \tag{2}$$

with C a temperature independent constant, α_S the volume fraction of semicrystalline regions, ϕ_L the local crystallinity of the semicrystalline regions, and d_c and d_a the temperature dependent mass densities of the crystalline and amorphous phases, respectively. In principle electron densities should be used but, as only PEO is left, this is accounted for by a constant conversion factor included in the constant C. In this model a uniformity of the stacking statistics over the different semicrystalline regions is assumed and the amorphous regions outside the stacks are considered not to contribute to the experimental scattering patterns.

ϕ_L is calculated from the correlation functions with the quadratic expression:

$$A = \phi(1-\phi)L_p \tag{3}$$

where A represents the intersection of the linear regression to the autocorrelation triangle with the abscissa, L_p, the long period, obtained from the position of the first sidemaximum in $K(x)$, and ϕ the (local) volume fraction (within the stacks) of the minority component. Independent information is needed to decide whether ϕ corresponds to ϕ_L or $(1-\phi_L)$. Here, the crystallinity values obtained from DSC are used as a guideline and ϕ was taken to be equal to the amorphous fraction, $(1-\phi_L)$, over the full time range. The crystalline, l_c, and the amorphous layer thickness, l_a, were calculated from the product of L_p with ϕ_L or $(1-\phi_L)$, respectively.

The factor $\phi_L(1-\phi_L)$ in Q_{id} can thus be obtained from the correlation functions. As a result α_S, C and $(d_c-d_a)^2$ are the only unknowns in Eq. (3). C and $(d_c-d_a)^2$ are time independent and the product $C(d_c-d_a)^2$ can be determined by assuming α_S to be equal to 1 at complete crystallization (after 40 min), and by using a scaling procedure [28]. Next, α_S, the only unknown left in Eq. (2), was determined over the full time range. The product $\alpha_S\phi_L$ equals the PEO volume fraction crystallinity (χ_v) with respect to the total PEO volume (the silicate volume is thus not included!). Using the mass densities of the amorphous and crystalline phases, the volume fraction crystallinity can be transformed into a mass fraction crystallinity χ_m.

$$\chi_m = \frac{1}{1+\frac{d_A}{d_C}\left(\frac{1-\chi_v}{\chi_v}\right)} \tag{4}$$

The calculated mass fraction crystallinity χ_m can be compared to the PEO mass fraction crystallinity obtained from DSC. For the crystalline and amorphous density, values of 1.21 and 1.13 were taken, respectively [30].

3.2. Wide-angle X-ray scattering (WAXS)

A linear background was subtracted from the time resolved WAXS data, collected over the angular range $7.7 \le 2\theta \le 66°$ (with 2θ the scattering angle). In this angular range the contribution of silicate layers to the WAXS patterns is negligibly small. The WAXS patterns corresponding to the crystallization of pure PEO are shown in Fig. 1. The peak around 24° is a combination of the PEO 112 and 032 reflections and the peak at 20° is from the 120 reflection [31]. The patterns

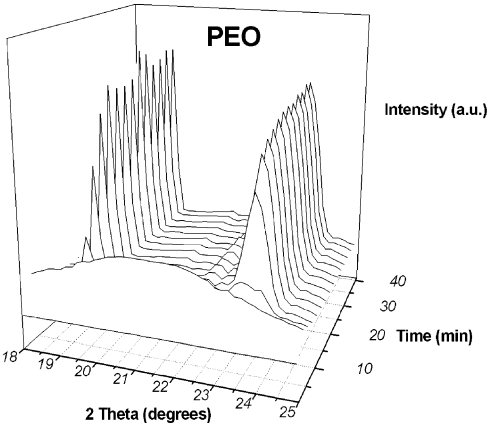

Fig. 1. WAXD patterns of PEO measured during isothermal crystallization at 48 °C. For clarity only one scattering pattern in 10 has been drawn.

were fitted using the Microcal™ Origin® data processing program to a linear combination of a Lorentz function for the amorphous halo and Pearson functions for the crystalline peaks.

Lorentz function:

$$y = y_0 + \left(2\frac{A}{\pi}\right)\left(\frac{w}{4(x-x_c)^2 + w^2}\right) \quad (5)$$

Pearson function:

$$y = y_0 + \frac{A}{\left(1 + 4\left(\frac{x-x_c}{w}\right)^2(2^{1/m}-1)\right)^m} \quad (6)$$

where y represents the measured intensity, A the peak area, w the peak width at half height, x_c the peak position and m the width at the foot of the peak.

Crystallinity values could not be calculated because the contribution of the amorphous halo is rather uncertain due to uncertainties in the background subtraction procedure. Therefore, a crystallinity index is reported, defined as the total integrated intensity of all crystalline peaks normalized to the total integrated intensity of all crystalline peaks at full crystallization.

The lateral dimension of a crystallite D_{hkl} in the direction perpendicular to the (hkl) reflecting planes was estimated from Sherrer's equation [32].

$$D_{hkl} = \frac{\lambda}{\beta_0 \cos\theta} \quad (7)$$

with D_{hkl} the crystallite size corresponding to a certain hkl reflection, λ the wavelength of the X-rays and β_0 the peak width at half height and θ half the scattering angle at the peak position. In this investigation the crystallite sizes corresponding to the 120 reflection were calculated.

4. Results and discussion

4.1. Nanocomposite morphology

The nature of the MMT morphology was deduced from the static scattering experiments. Fig. 2 shows the curves of pure (surfactant modified) MMT, pure PEO and of the PEO/MMT nanocomposites with 1, 2, 4 and 10 wt% MMT. The curve of pure MMT shows a strong peak at $2\theta = 2.7°$, corresponding to the interlayer distance of the silicate layer stacks and equal to 32 Å. The surfactants already increase the interlayer distance considerably in this case compared to pure MMT (not shown). The PEO/MMT nanocomposites show peaks at $2\theta = 2.2°$, corresponding to an interlayer distance of 40 Å. The increase in interlayer distance points to the intercalation of polymer chains between the silicate layers. So, at least part of the PEO/MMT nanocomposites—if not all—is of the intercalated type. In principle, it cannot be deduced from the scattering patterns whether or not also part of the MMT is exfoliated. Exfoliated MMT no longer displays a peak, contributes to the scattering pattern as isolated platelets do (form factor only) and would be hardly distinguishable form the background. The extent of exfoliation is, however, believed to be moderate because the peaks of the PEO/MMT nanocomposites are very sharp, even sharper than for the pure clay peak. In the case of partially exfoliated MMT layers, the scattering peak would appear broader due to the paracrystalline distortions associated with the presence of a broad interlayer distance spectrum with values between intercalated and fully exfoliated.

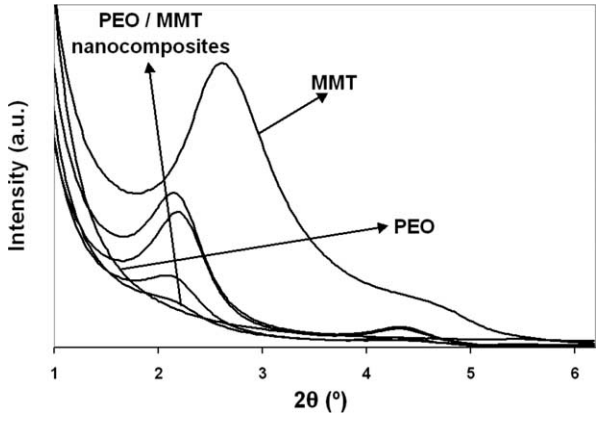

Fig. 2. Scattering patterns of PEO, MMT and PEO/MMT nanocomposites.

4.2. DSC crystallization behavior

Fig. 3 shows the DSC exothermic curves of pure PEO and the PEO/MMT nanocomposites during crystallization at 48 °C. The curves have been shifted vertically for clarity.

All curves display an unimodal crystallization peak, except for the sample with 1% MMT that clearly exhibits two maxima. The second maximum (at about 9 min) and in fact the entire curve at times beyond that maximum closely resembles that of pure PEO, suggesting their common origin. Therefore, these maxima are connected with a dashed line in Fig. 3. At about 4 min another maximum is present that has no counterpart in the pure PEO curve. The onset of this early peak virtually coincides with the time at which the isothermal temperature is reached and this also holds for the (single) peaks associated with the other composites. Accordingly assuming their common origin, these peaks are connected by a dotted line

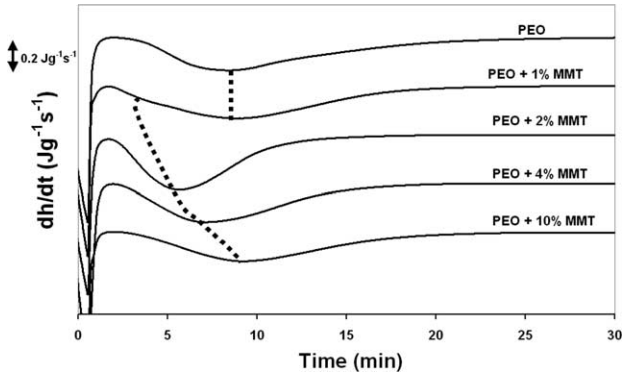

Fig. 3. Isothermal DSC crystallization curves of PEO and PEO/MMT nanocomposites. The isothermal crystallization temperature is 48 °C. The dashed and dotted lines are explained in the text.

in Fig. 3. The maxima of the latter peaks, however, shift to later times with increasing MMT contents. As a result the (overall) crystallization half-times first shift towards lower times for PEO + 1 and + 2 wt% MMT with increasing MMT wt%, but increases again for PEO + 4 wt% MMT and PEO + 10 wt% MMT. The overall mass fraction crystallinity, calculated from the integrated DSC peak areas and corrected for the percentage PEO, is 62% for PEO and about 65% for the PEO/MMT nanocomposites.

The bimodal crystallization behavior associated with the 1% MMT sample indicates the MMT is not well dispersed over the sample volume. In some volumes there is MMT present whereas in others there is hardly any. In the latter case crystallization occurs (locally) similar to pure PEO (PEO peak at about 9 min). The early peak corresponds to volumes where MMT is present (composite peak) and it is clear from the decrease in onset time of crystallization that the silicate layers act as nucleating agents for the crystallization of PEO. At higher MMT contents the MMT is homogeneously dispersed over the sample (mainly due to the higher amount) and as a result the pure PEO peak disappears. However, the (single) composite peak progressively shifts to higher times with increasing MMT contents, pointing at a decrease of the overall crystallization rate. The overall crystallization rate is proportional to both the (primary) nucleation rate and the crystal/spherulite growth rate. The constancy of the crystallization onset time suggests that the nucleating ability is not affected and accordingly the decrease in overall crystallization rate points at a progressively decreasing crystal/spherulite growth rate. At the lowest MMT concentrations, the influence of the silicate layers as nucleating agents dominates, while at higher concentrations the influence of the silicate layers as growth retarders becomes more important. As a result a maximum in the overall crystallization rate appears at PEO + 2 wt% MMT. A similar crystallization behavior was observed for PA-6/MMT nanocomposites as explained in the introduction [20,21].

4.3. Spherulitic growth

The spherulite growth during isothermal crystallization at 48 °C was obtained from light microscopy (LM) measurements. Due to its heterogeneous nature, the sample with 1% MMT was discarded. In all considered cases spherulites could be grown that reach several 100 μm in diameter. It was noticed, however, that the final diameter becomes larger for thinner samples in contrast to the growth rate, which is hardly affected. This is expected as the primary nuclei are progressively diluted in the narrowing two-dimensional confinement realized by the glass plates. Simple compression molding does not allow for an accurate control of the sample thickness and as a result these LM images cannot be used safely to address the nucleation density. It has been described that the glass plate confinement may also reduce the spherulite growth rate compared to that of the bulk (i.e. three-dimensional growth) [33]. The invariance of the observed growth rates with sample thickness, however, suggest that such effects are negligible in the present case.

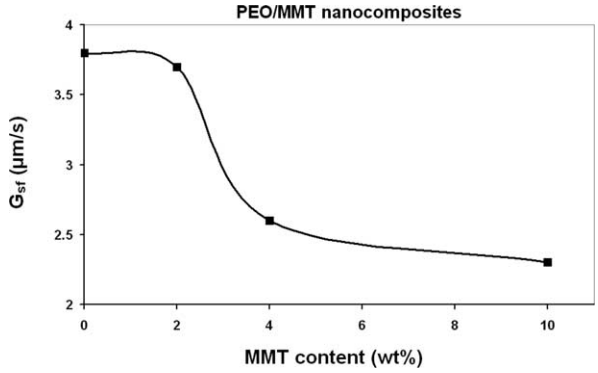

Fig. 4. Spherulite growth rate (G_{sf}) as a function of the MMT content in the PEO/MMT nanocomposites during isothermal crystallization at 48 °C.

The spherulite growth rates (displayed in Fig. 4) of PEO and PEO + 2% MMT are virtually identical, but decrease considerably for the PEO/MMT nanocomposites with a higher MMT content. This decrease of spherulite growth rate is in agreement with the DSC based expectations.

4.4. Semicrystalline structure development

4.4.1. SAXS

SAXS scattering patterns were taken every 15 s during isothermal crystallization at 48 °C. The corresponding evolution of L_P, l_c, l_a and the volume fraction of semicrystalline material, χ_v, with time is given in Fig. 5. Again, due to its heterogeneous nature, the sample with 1% MMT was discarded. Furthermore, nor the sample with 10% MMT is included as mentioned in the data analysis (Section 3.1).

The onset times of crystallization and the overall crystallization time of the PEO/MMT nanocomposites (with 2 and 4% MMT), to be read from the evolution of χ_v in Fig. 5(d), are shorter compared to the pure PEO times, confirming again the nucleating ability of the silicate layers.

The long periods of pure PEO and the PEO/MMT nanocomposites are identical within experimental error. There seem to be systematic differences in l_c and l_a but given the important (MMT content dependent) background corrections (essentially imparting changes to the scattering in the Porod region that are reflected in the autocorrelation triangle of the correlation functions) we consider these as not too serious. Moreover, the value of the long period is not affected by the background correction and exactly these values are sample independent! The differences between PEO and the PEO/MMT nanocomposites relative to each other are, therefore, most likely not due to true morphological differences. So, it can be concluded that the silicate layers enhance primary nucleation and disturb the growth of the semicrystalline stacks but do not affect the stack internal structure.

The long period, the crystal layer thickness and the amorphous layer thickness of pure PEO and the PEO/MMT nanocomposites do not change during the whole crystallization process. Apparently, the increase in semicrystalline material is caused by lateral stack growth, while the stack internal

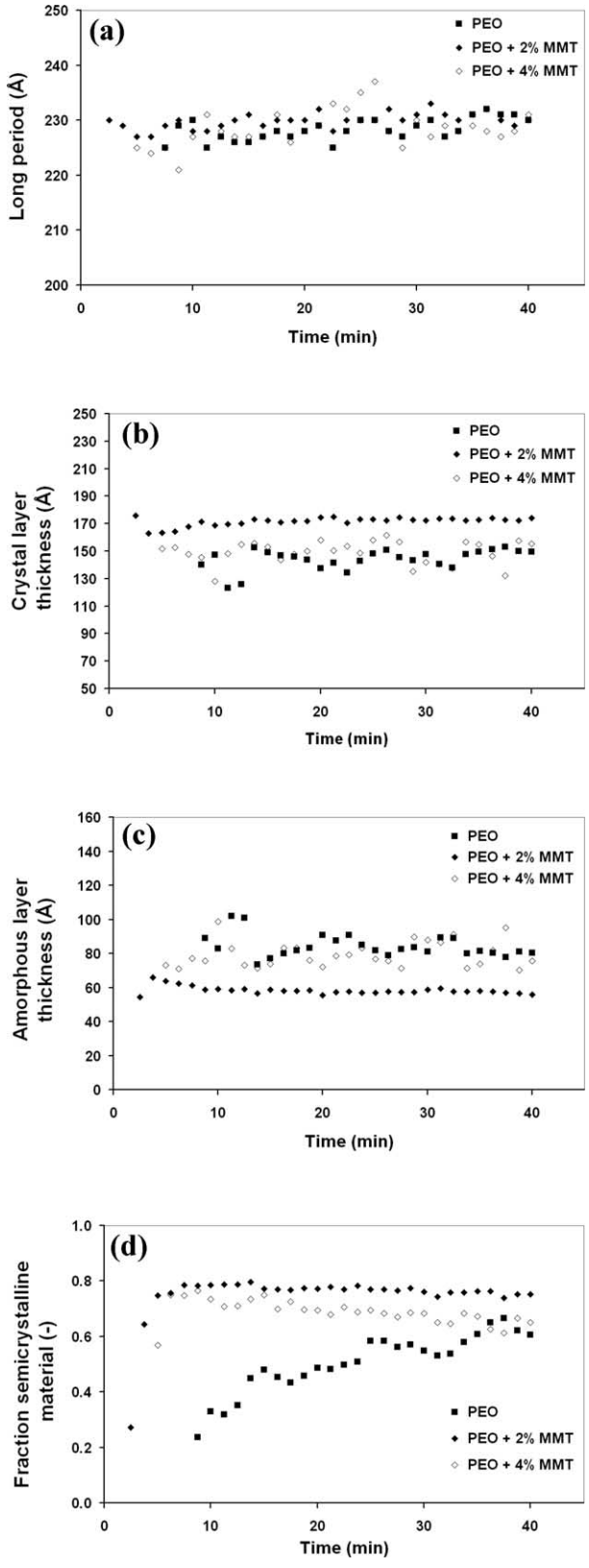

Fig. 5. The long period (a), crystal layer thickness (b), amorphous layer thickness (c) and the volume fraction semicrystalline material (d) of pure PEO and the PEO/MMT nanocomposites with 2 and 4% MMT as a function of time during isothermal crystallization at 48 °C. For clarity, only one measurement point in five has been drawn.

Table 1
Comparison of mass fraction crystallinities of pure PEO and the PEO/MMT nanocomposites calculated from SAXS and DSC

Material	SAXS cryst. (%)	DSC cryst. (%)
PEO	63±5	62
PEO+2% MMT	78±4	65
PEO+4% MMT	70±11	65

The SAXS crystallinity is an average calculated from the scattering patterns taken between 10 and 40 min for the PEO/MMT nanocomposites and 30–40 min for PEO.

structure in terms of crystalline and amorphous layer thickness remains constant. In other words the crystallinity increase is related to an increase of α_S, rather than of ϕ_L.

The SAXS volume fraction crystallinity values reached at the end of the crystallization, have been converted to mass fraction crystallinity values (Section 3.1) and compared to the crystallinity values calculated from the DSC crystallization curves. The crystallinity values of both techniques are depicted in Table 1. The SAXS overall mass fraction crystallinity closely resembles that of DSC, justifying the assumption that the minority component ϕ equals $(1-\phi_L)$. The agreement is quite good for pure PEO and the deviations found for the nanocomposites are likely due to the mentioned uncertainties in the SAXS background subtraction procedure.

4.4.2. WAXS

The development of the WAXS crystallinity index is shown in Fig. 6. The difference between pure PEO and the PEO/MMT nanocomposites is clear. The crystallinity index of the PEO/MMT nanocomposites starts to increase sooner and increases faster than that of pure PEO. The WAXS experiments confirm the observations from the DSC measurements that the silicate layers function as nucleating agents for the crystallization of the PEO. The small difference in crystallization kinetics between PEO+2% MMT and +4% MMT is reflected in the WAXS indices too.

The Debye–Sherrer crystal size (D_{hkl}) remains fairly constant during crystallization and close to 400 Å independent on whether or not MMT is involved. The Debye–Sherrer crystal size is a measure of size but is also influenced by

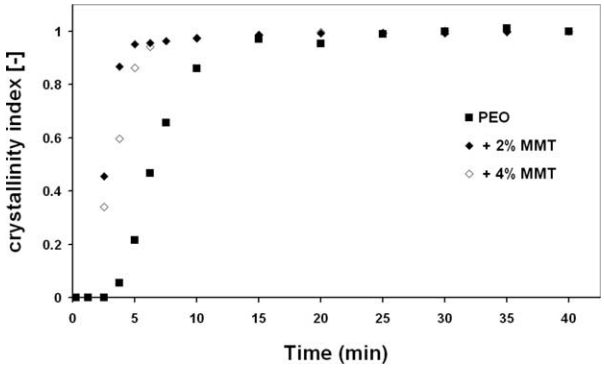

Fig. 6. WAXD crystallinity indexes of pure PEO and PEO/MMT nanocomposites with 2 and 4% MMT as a function of time during isothermal crystallization at 48 °C.

disorder. So, it can be concluded that the silicate layers do not influence the size or perfection of the crystals.

5. Conclusions

From the earlier crystallization onset in the isothermal DSC experiments and in the SAXS and WAXS crystallinity estimates it was concluded that the silicate layers act as nucleating agents for the crystallization of PEO. Furthermore, at a sufficiently high amount the silicate layers retard the crystal growth as could be derived from the decrease of the overall crystallization rate and the decrease of the spherulite growth rate at high MMT contents.

There seems to be a clear trend in the influence of silicate layers on the crystallization behavior of polymer nanocomposite matrices despite their differences in resulting nanocomposite morphology. The changes in the crystallization behavior of PEO as matrix material in the present intercalated nanocomposites are very similar to those in exfoliated PA-6/MMT nanocomposites [20,21,23], where also a two-fold influence (nucleating ability and growth retardation) of the silicate layers on the crystallization behavior was detected. The balance between these two opposing effects determines the overall crystallization rate of the polymer matrix. At lower MMT concentrations, the increased amount of nucleating sites enhances the crystallization kinetics, while at higher MMT concentrations, the increased amount of retarding impurities slows down the crystallization. In the latter case, the silicate layers are non-crystallisable barriers in the crystallization of the polymer matrix, which disturb laterally growing crystalline lamellae. Another possibility is that a decrease in crystal growth rate is caused by silicate layers through their hindrance on polymer chain motion. This disturbed crystal growth, however, does not result in visible changes to the semicrystalline stack morphology or the crystal perfection.

Acknowledgements

The authors would like to thank the Fund for Scientific Research-Flanders (Belgium), as well as the Research Council KULeuven for the financial support of this research; one of them (B.G.), is a postdoctoral fellow of the Fund for Scientific Research-Flanders. The authors also would like to acknowledge the Dutch-Belgian beamline (DUBBLE) research group at the ESRF, Grenoble, France, for their help and support with the time-resolved small angle X-ray experiments.

References

[1] Alexandre M, Dubois P. Mater Sci Eng 2000;28(1–2):1–63.
[2] Giannelis EP, Krishnamoorti R, Manias E. Adv Polym Sci 1999;138:107–47.
[3] Lincoln DM, Vaia RA, Wang Z-G, Hsiao BS. Polymer 2001;42:1621–31.
[4] Lepoittevin B, Devalckenaere M, Pantoustier N, Alexandre M, Kubies D, Calberg C, et al. Polymer 2002;43(14):4017–23.
[5] Pantoustier N, Lepoittevin B, Alexandre M, Kubies D, Calberg C, Jerome R, et al. Polym Eng Sci 2002;42(9):1928–37.
[6] Maiti P, Nam PH, Okamoto M, Hasegawa N, Usuki A. Macromolecules 2002;35:2042–9.
[7] Moussaif N, Groeninckx G. Polymer 2003;44:7899–906.
[8] Wunderlich B. Macromolecular physics. vol. 2. New York: Academic Press; 1976 [chapter 5].
[9] Groeninckx G, Berghmans H, Overbergh N, Smets GJ. Polym Sci, Polym Phys Ed 1974;12:303–16.
[10] Wu TM, Chen EC. Polym Eng Sci 2002;42(6):1141–9.
[11] Wu TM, Wu JY. J Macromol Sci, Phys 2002;B41(1):17–31.
[12] Maiti P, Nam PH, Okamoto M, Kotaka T, Hasegawa N, Usuki A. Polym Eng Sci 2002;42(9):1864–71.
[13] Kamal MR, Borse NK, Garcia-Rejon A. Polym Eng Sci 2002;42(9):1883–96.
[14] Liu X, Wu Q. Polymer 2002;43:1933–6.
[15] Liu X, Wu Q. Eur Polym J 2002;38:1383–9.
[16] Medellin-Rodriguez FJ, Burger C, Hsiao BS, Chu B, Vaia RA, Phillips S. Polymer 2001;42:9015–23.
[17] Priya L, Jog JP. J Polym Sci, Part B: Polym Phys 2002;40:1682–9.
[18] Lincoln DM, Vaia RA, Wang ZG, Hsiao BS, Krishnamoorti R. Polymer 2001;42:9975–85.
[19] Xu W, Ge M, He P. J Polym Sci, Part B: Polym Phys 2002;40:408–14.
[20] Fornes TD, Paul DR. Polymer 2003;44:3945–61.
[21] Van Es M. Polymer-clay nanocomposites. PhD thesis. The Netherlands: Technical University of Delft. ISBN 90 77017 27 5; 2001 [chapter 7].
[22] Homminga D, Goderis B, Reynaers H, Dolbnya I, Groeninckx G. Crystallization behavior of polymer/montmorillonite nanocomposites. Part II. Intercalated poly(ε-caprolactone)/montmorillonite nanocomposites 2005.
[23] Homminga D, Goderis B, Reynaers H, Mathot VBF, Groeninckx G. Crystallization behavior of polymer/montmorillonite nanocomposites. Part III. Polyamide-6/montmorillonite nanocomposites, influence of matrix molecular weight, and of montmorillonite type and concentration 2005.
[24] Khanna YP, Reimschuessel AC, Banerjie A, Altman C. Polym Eng Sci 1988;28(24):1600–6.
[25] Khanna YP, Kumar R, Reimschuessel AC. Polym Eng Sci 1988;28(24):1607–11.
[26] Odian G. Principles of polymerization. 3rd ed. Wiley: New York; 1991 [chapter 7].
[27] Athas Databank, URL: http://web.utk.edu/~athas/databank/Intro.Html, last revision February 5; 2000.
[28] Goderis B, Reynaers H, Koch MHJ, Mathot VBF. J Polym Sci, Part B: Polym Phys 1999;37:1715–38.
[29] Strobl GR, Schneider M. J Polym Sci, Polym Phys Ed 1980;18:1343–59.
[30] Brandrup J, Immergut EH. Polymer handbook. 3rd ed. New York: Wiley; 1989 [chapter 6].
[31] Bortel E, Hodorowicz S, Lamot R. Makromol Chem 1979;180:2491–8.
[32] Alexander LE. In: Robert E, editor. Diffraction methods in polymer science. Hunington, New York: Krieger Publishing Company; 1979. p. 423.
[33] Wunderlich B. Macromolecular physics. vol. 2. New York: Academic Press; 1976 [chapter 6].